LETTER

Design of a feasible high-efficiency ^{63}NiO/ZnO integrated betavoltaic battery

To cite this article: Xinxu Yuan *et al* 2023 *Appl. Phys. Express* **16** 021006

View the article online for updates and enhancements.

Design of a feasible high-efficiency ^{63}NiO/ZnO integrated betavoltaic battery

Xinxu Yuan[1], Jingbin Lu[1*], Renzhou Zheng[1*], Xue Zhang[1], Ziyi Chen[1], Xiaoyi Li[1], Chengqian Li[1], Yumin Liu[2], Lei Liang[3,4,5], and Zhigang Song[6]

[1]College of Physics, Jilin University, Changchun, 130012, People's Republic of China
[2]College of Nuclear Science and Engineering, East China University of Technology, Nanchang 330013, Jiangxi, People's Republic of China
[3]State Key Laboratory of Luminescence and Applications, Changchun Institute of Optics, Fine Mechanics and Physics, Chinese Academy of Sciences, Changchun 130033, Jilin, People's Republic of China
[4]Daheng College, University of Chinese Academy of Sciences, Beijing 100049, People's Republic of China
[5]Peng Cheng Laboratory, Shenzhen 518000, Guangdong, People's Republic of China
[6]Institute of Semiconductors, Chinese Academy of Sciences, Beijing100083, People's Republic of China

*E-mail: ljb@jlu.edu.cn; zhengrz20@mails.jlu.edu.cn

The conventional betavoltaic battery design fails to eliminate the inherent influence of the radioactive source self-absorption effect, leading to a bottleneck in the efficiency and power of betavoltaic batteries. In this paper, a feasible high-efficiency ^{63}NiO/ZnO integrated betavoltaic battery is designed and compared with the conventional betavoltaic battery. Simulation results show that the proposed betavoltaic battery has better output performance and breaks the upper limit of efficiency and power. The work presented here provides valuable insights for radioisotope battery designs, and the physical modeling procedure discussed can serve as a good reference for further applications in simulating heterojunctions of type-II semiconductors. © 2023 The Japan Society of Applied Physics

Supplementary material for this article is available online

The betavoltaic battery, which converts decay energy into electrical energy, consists mainly of a beta-emitting material (energy-carrying unit) and a junction device (transducer unit).[1] The betavoltaic battery has stable output electrical performance, a long lifetime, and high energy density.[2] Thus, the betavoltaic battery is considered to have wide prospects for application in remote wireless sensors,[3] biomedical implanted devices,[4] and other fields. However, due to the low efficiency and power of betavoltaic batteries, their applications are limited to micro/nanoelectro-mechanical systems (M/NEMS).[5,6]

The main reason that affects and limits the efficiency and power of betavoltaic batteries is the self-absorption effect of radioactive sources. At present, the related research has focused on optimizing the structure of the transducer to reduce the energy loss of radioactive sources, such as covered source betavoltaic batteries,[7] nanowire betavoltaic batteries[8] and multi-well structure betavoltaic batteries.[9] Innovative structural designs such as these can improve electrical performance to some extent, but these designs do not break the bottleneck of power and efficiency. The underlying reason is that the energy-carrying unit and transducer unit of betavoltaic batteries is separated, which means that the inherent effect of radioactive source self-absorption always limits the efficiency and power of the betavoltaic batteries.

Therefore, in the field of betavoltaic batteries, there is an urgent need for a feasible design scheme to solve the problem of the self-absorption effect, while taking into account the service life, cost, and safety. ^{63}Ni is usually used as the source of betavoltaic batteries due to its soft beta spectrum ($E_{avg} = 17\,\mathrm{keV}$, $E_{max} = 67\,\mathrm{keV}$) and long half-life ($T_{1/2} = 100$ years).[10] In 2020, Yu Wang et al. theoretically proposed a ^{63}NiO/Si heterojunction betavoltaic battery that can solve the drawback of the radioactive source self-absorption effect.[11] And the mass number of ^{63}Ni is very close to the standard relative atomic mass (58.693) of nickel. Therefore, we believe that the difference caused by the

isotope effect is small, so that ^{63}NiO can exert the same physical properties as NiO semiconductors.

Herein, based on the consideration of all factors in the design of betavoltaic batteries, we propose a high-efficiency ^{63}NiO/ZnO integrated betavoltaic battery. The Silvaco ATLAS software was used to build a full physical model to simulate NiO/ZnO type-II heterojunction. And Monte Carlo simulation was used to simulate the emission and deposition behavior of beta particles. On the one hand, the proposed structure consists of two wide bandgap semiconductor materials with high radiation hardness, which guarantees the lifetime of the battery. On the other hand, the preparation process of NiO/ZnO heterojunction is simple, and the constituent elements are cheap and abundant in the natural environment.[12] Therefore, the ^{63}NiO/ZnO betavoltaic battery proposed in this paper has excellent application prospects and it is very desirable to be prepared in the process, such as the sol-gel method.[13]

The actual schematic representation of NiO/ZnO separate betavoltaic is shown in Fig. 1(a). The red wireframe area is the structure diagram of the separate device, containing a 100 mCi · cm^{-2} radioactive source and a NiO/ZnO heterojunction. The ^{63}NiO/ZnO integrated betavoltaic battery is shown in Fig. 1(b). In Figs. 1(a) and 1(b), Au and Ti/Au contact schemes were used for the anode and cathode, respectively. During model building, only the semiconductor transducer unit is considered and the electrodes are ideal ohmic contacts.

The electrical parameters of the NiO and ZnO semiconductors are presented in Table SI (see the supplementary data for details), and ^{63}NiO used the same physical parameters as NiO during the simulation. Due to the very low mobility of NiO carriers, p-type NiO layers are usually used to obtain the built-in electric field and the volume proportion of the NiO layer in the whole junction device is also small.[14] Nevertheless, in the structural design of betavoltaic batteries, the position of the depletion region must match the energy deposition of beta particles emitted from radioactive sources.
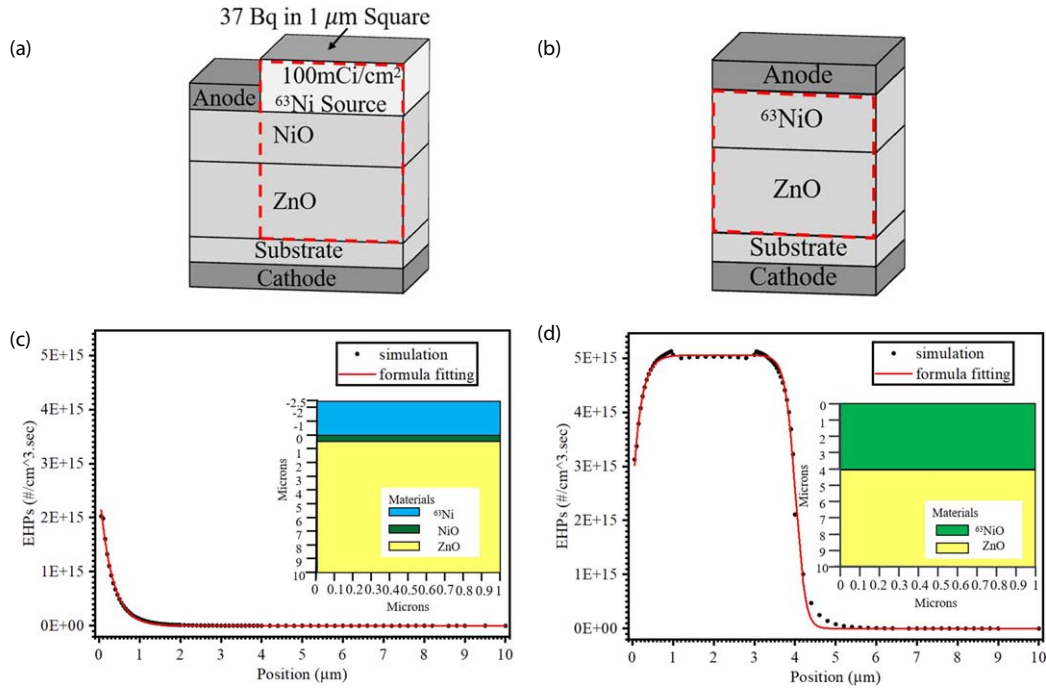
Fig. 1. (Color online) Schematic representation of betavoltaic battery structure (a) separate device (b) integrated device. Electron-hole pairs generation rate distributions in (c) separate device and (d) integrated device (the insets show the 2D model structure used in the TCAD simulation).

Therefore, in this work, p-type NiO was used as the emitter layer and n-type ZnO was used as the base layer, as shown in Figs. 1(a) and 1(b).

The distribution of the EHPs generation rate is shown in Fig. 1(c). And the inset is the 2D device structure applied in the simulation, and the ordinate direction is the incident depth, corresponding to the red wireframe region in Fig. 1(a). Since the total thickness of the battery transducer unit is 10 μm, the energy of beta particles emitted from the ^{63}Ni radioactive source can be deposited completely. The EHPs generation rate distribution exhibits an e-exponential decay law with incident depth, which can be fitted well by Eq. (1) and the red curve of the formula fitting is shown in Fig. 1(c).

$$G_1(y) = \frac{E_1(y)}{E_{ehp}} = \frac{G_1}{E_{ehp}} \exp(\alpha_1 \cdot y) \qquad (1)$$

The EHPs generation rate distribution curve in ^{63}NiO/ZnO devices is shown in Fig. 1(d). The thickness ranging from 0 to 4 μm corresponds to the ^{63}NiO layer. The EHPs distribution curve can be fitted well using Eq. (2), as shown by the red curve of the formula fitting in Fig. 1(d).

$$
\begin{aligned}
G_2(y) &= \frac{E_2(y)}{E_{ehp}} \\
&= \frac{G_2}{E_{ehp}((b + c \cdot \exp(y^2)) + d \cdot \exp(\alpha_2 \cdot y))}
\end{aligned} \qquad (2)
$$

In Eqs. (1) and (2), $E_1(y)$ and $E_2(y)$ are the energy deposition rate, E_{ehp} is the average energy dissipated per electron-hole pair generated, (for NiO/^{63}NiO, it is 10.58 eV; for ZnO, it is 9.74 eV),[15] G_1, G_2, α_1, α_2, b, c, and d are the fitting parameters.

The power density of the surface (contacts with the transducer unit) of the ^{63}NiO source and ^{63}Ni source as a function of the source thickness is shown in Fig. 2(a). The geometric dimensions of the two sources are the same, but the purity of ^{63}Ni radioisotopes is different. When the thickness of the source is 2 μm, the apparent power density of both sources reaches saturation, as shown in Fig. 2(a). Hence, this saturation thickness is usually considered as the optimal source thickness, and the optimal thickness is independent of the source purity, which is in agreement with the calculation results of Sergey et al.[16]

The relationship between the total activity and the thicknesses of the ^{63}NiO source and ^{63}Ni source is shown in Fig. 2(b). The activity of the ^{63}Ni source is 100.85 mCi·cm^{-2} when it reaches the optimum thickness, which corresponds to the ^{63}NiO source thickness of 3.27 μm. The activity of the ^{63}NiO source is 61.70 mCi·cm^{-2} when it reaches the optimum thickness, which corresponds to the ^{63}Ni source thickness of 1.22 μm. The 61.70 mCi·cm^{-2} was determined as saturated activity, which is related to the optimum thickness.

According to Anderson's electron affinities rule, a schematic diagram of the theoretical NiO/ZnO type-II heterojunction energy band is given in Fig. 2(c).

The Blaze simulator is used for simulating NiO/ZnO heterojunction devices. For accurately simulating the NiO/ZnO type-II heterojunction device, various physical models are applied, including the Shockley–Read–Hall (SRH), the thermionic emission, the Danielsson model, the Fermi–Dirac statistics, the Parallel Electric Field Dependence (FLDMOB) model, the Bandgap Narrowing (BGN) model, the band–band recombination (OPTR) for NiO and ZnO direct materials,[17,18] and the high field mobility model (OZGUR. N) of ZnO.

In the TCAD simulation, the thermionic emission and Danielsson model were considered to describe the interfacial
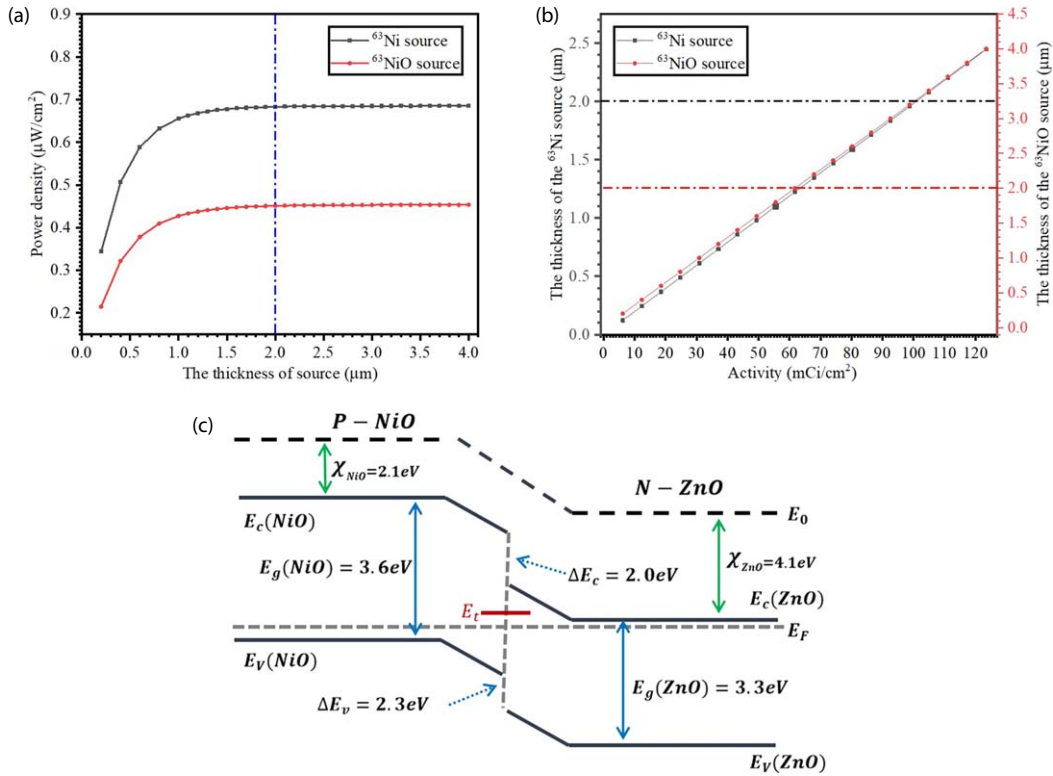
Fig. 2. (Color online) (a) Schematic representation of the source apparent power density as a function of source thickness; (b) Correlation between source activity and source thickness (the ^{63}Ni and ^{63}NiO sources are rectangular sources with area $1 \times 1~\mu m^2$). (c) Energy band diagram of NiO/ZnO heterojunction (the χ is the electron affinity energy, E_g is the bandgap width, E_0 is the vacuum level, E_F is the Fermi level, E_c is the conduction band level, E_v is the valence band level, E_t is the trap level at the interface, ΔE_c is the conduction band discontinuity and ΔE_v is valence band discontinuity).

states of the NiO/ZnO heterojunction. The thermionic emission mechanism is a boundary condition to keep the current continuity at the interface of the abrupt heterojunction.[19] The Danielsson model affected the recombination of electrons and holes on both sides of type-II heterojunction.[20] At the node points along the interface of the heterojunction, the recombination rate combining the thermionic emission and Danielsson model is given by:[21]

$$U_{Dan} = \frac{(N_{ZnO}P_{NiO} - N_{ZnO}^{eq}P_{NiO}^{eq})}{(N_{ZnO}+N_{ZnO}^{eq}a_0) + (P_{NiO}+P_{NiO}^{eq}/a_0)} \tag{3}$$

$$a_0 = \exp\left(\frac{E_t - E_F}{kT}\right) \tag{4}$$

where N and P are the electron and hole concentrations and their equilibrium values by N_{eq} and P_{eq}. The k is the Boltzmann constant, T is the lattice temperature and E_t–E_F is set to -0.1 eV.

Firstly, the junction depth and doping concentration of separate betavoltaic batteries are optimized to achieve higher output power. The J–V characteristics of the separate device with different NiO layer thicknesses are shown in Fig. 3(a). The results show that the smaller the thickness of the NiO layer, the greater the current density of the battery. The reason is that the penetration of beta particles emitted by the ^{63}Ni source is limited, and most of the energy is deposited in the shallow layer in the junction device, as shown in Fig. 1(c). And the carrier recombination rate is the lowest

at the interface between NiO and ZnO material as shown in Fig. 3(b). This indicates that the position of the depletion region is related to the thickness of NiO. Therefore, when the thickness of the NiO layer is smaller, the depletion region of the transducer unit matches the energy deposition range better. According to the research work of Namseok Park et al., the single-preparation NiO film by sol-gel spinning is 0.05 μm.[22] Therefore, we chose 0.05 μm as the optimized value for the junction depth.

The P_m is plotted as a function of doping concentrations in Fig. 4(a). The results show that when the N region is lightly doped, the larger the doping concentration of the P region, the higher the P_m of the battery. According to the study of S. C. Chen et al. the carrier mobility of Cu-doped NiO decreases with increasing doping concentration.[23] Nevertheless, the carrier mobility invoked by our model is fixed in simulation. Therefore, we choose $N_a = 1.0$ E $+ 19$ cm^{-3} and $N_d = 3.07$ E $+ 14$ cm^{-3} as the final optimized doping concentration, and FF is 85.1046% in this case, as shown in Fig. 4(b), indicates that the battery has excellent electrical performance.

For discussion of the influence of the self-absorption effect, the activity of the energy-carrying unit of both batteries was kept constant, and the overall device size was kept consistent to compare the output electrical performance. The P_m of the separate device and integrated device are shown in Fig. 5(a). The value of the separate device no longer increases significantly when the activity of the source exceeds 61.70 mCi·cm^{-2} and does not reach the saturated activity (100.85 mCi·cm^{-2}). In contrast, even if the activity
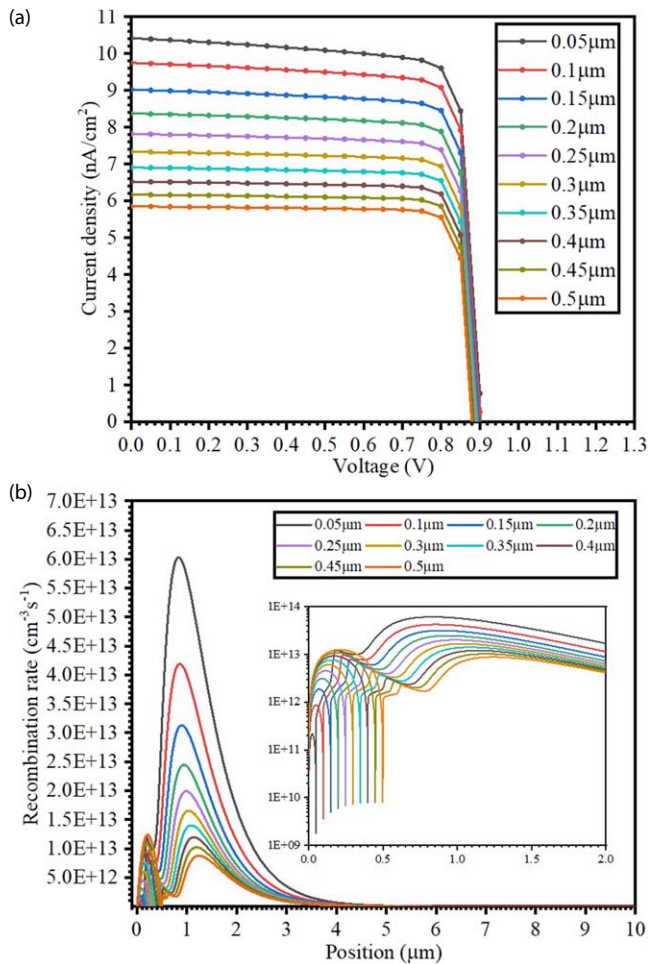
Fig. 3. (Color online) The (a) *J–V* characteristics and (b) recombination rate of separate device (the simulation diagram of the separated device is the inset in Fig. 1(c), in this part of the simulation, the ^{63}Ni source thickness is 2 μm, the doping concentration of P region is 1.0 E + 19 cm^{-3} and the doping concentration of N region is 1.0 E + 16 cm^{-3}).

Fig. 4. (Color online) The (a) P_m and (b) *FF* of the separate device versus doping concentrations in the P region and N region (the N_a is the doping concentration of the P region and the N_d is the doping concentration of N region).

of the integrated device reaches saturated activity (61.70 mCi·cm^{-2}), the electrical performance of the integrated device continues to increase. This indicates that the integrated device can break through the power ceiling caused by the self-absorption effect.

The simulated energy band structures of the separate device and integrated device are shown in Fig. 5(b). The results show that the depletion region of the battery mainly exists inside the ZnO material, in the range of about 2 μm close to the interface. However, when the ^{63}NiO layer thickness of the integrated device changes, the location of the depletion region always changes, which means that the extent of the depletion region always matches the energy deposition of the beta particles entering the integrated device. Therefore, the integrated device greatly improves energy conversion efficiency. The recombination rate distributions of the separate device and integrated device are shown in Fig. 5(c). At the material interface, the recombination rate of the integrated device is significantly higher than that of the separated device. This is due to the large number of EHPs produced by the ^{63}NiO material in the integrated device due to its own energy deposition, as shown in Fig. 1(d). According to thermionic emission and Danielsson model, tunneling recombination occurs when a large number of

electrons and holes exist on both sides of the type-II band heterogenous interface, leading to an increase in recombination rate at the interface.

It can be observed from the current density distribution of the two types of batteries in Fig. 5(d) that the total current density of integrated devices is greater. This is consistent with the results in Table I, when the activity is 123.40 mCi·cm^{-2}, the J_{sc} of the integrated device is 11.48 nA·cm^{-2}, which is 10 times higher than that of the separate device. The results show that the integrated device generates more charge carriers, which improves the energy utilization rate of the energy-carrying.

In summary, The comparison of output performance between separate and integrated devices is presented in Table I and the integrated device has better electrical performance. When the activity reaches saturation activity (61.70 mCi·cm^{-2}), the η of the integrated device is 14.52%, and the η of the separate device is only 1.27%. When the activity is 123.40 mCi·cm^{-2}, the η of the integrated device reached 21.8%, which is 17 times higher than that of the separate device. The results show that integrated device can eradicate the self-absorption effect, and break through the bottleneck of efficiency and power. Therefore, the integrated design method we proposed points out the direction for radioisotope batteries to use radioactive sources more rationally and efficiently. Furthermore, the model established in this work can be applied to other type-II semiconductor heterojunctions, such as $\beta-Ga_2O_3$/NiO, NiO/CeO$_2$, etc.
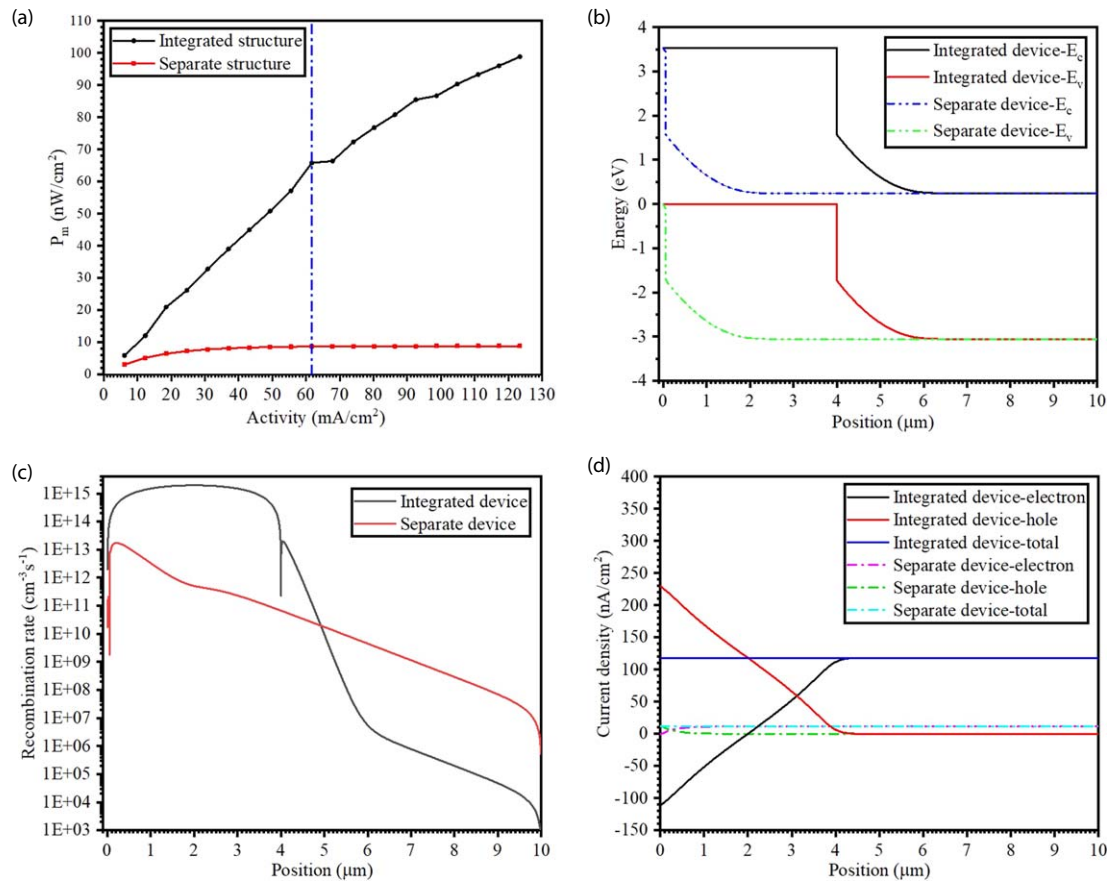
Fig. 5. (Color online) (a)The P_m versus activity in the separate device and integrated device (the simulation diagram of the integrated device is the inset in Fig. 1(d), in this part of the simulation, the doping concentration of the two types of batteries is set to $N_a = 1$ E + 19 cm^{-3} and $N_d = 3.07$ E + 14 cm^{-3}, and the NiO layer thickness of the separate device was fixed at 0.05 μm). The diagram of internal physical parameters of the separate device and integrated device with an activity of 123.40 mCi · cm^{-2} (b) energy band structure, (c) recombination rate, (d) current density distribution.

Table I. Comparison of output performance between separate and integrated devices.

Structure	Activity (mCi cm^{-2})	J_{sc} (nA cm^{-2})	V_{oc} (V)	(P_m) (nW cm^{-2})	FF (%)	η (%)
Separate device I	61.70	11.30	0.90	8.70	85.12	1.27
Separate device II	123.40	11.48	0.90	8.84	85.10	1.29
Integrate device I	61.70	79.26	0.95	65.83	86.98	14.52
Integrate device II	123.40	118.41	0.96	98.86	86.86	21.80

1) L. C. Olsen, NASA. LERC. Proc. of the 12th Space Photovoltaic Research and Technology Conf., 1993, p. 256.
2) M. Chandrashekhar, R. Duggirala, M. G. Spencer, and A. Lal, Appl. Phys. Lett. **91**, 053511 (2007).
3) R. Duggirala, H. Li, and A. Lal, Appl. Phys. Lett. **92**, 154104 (2008).
4) Y. Lei, Y. Yang, G. Li, Y. Liu, J. Xu, X. Xiong, S. Luo, and T. Peng, Appl. Phys. Lett. **116**, 153901 (2020).
5) B. Liu, K. P. Chen, N. P. Kherani, and S. Zukotynski, Appl. Phys. Lett. **95**, 233112 (2009).
6) C. Zhao, A. Liu, S. Bai, and Y. Zhao, Appl. Phys. Lett. **117**, 193901 (2020).
7) A. Krasnov, S. Legotin, K. Kuzmina, N. Ershova, and B. Rogozev, Nucl. Eng. Technol. **51**, 1978 (2019).
8) D. Wagner, D. Novog, and R. LaPierre, J. Appl. Phys. **127**, 244303 (2020).
9) Y. J. Yoon, J. S. Lee, I. M. Kang, J. H. Lee, and D. S. Kim, Nucl. Eng. Technol. **53**, 1284 (2021).
10) Z. Guoping, Z. Jianliang, and K. Guotu, Appl. Radiat. Isot. **82**, 119 (2013).
11) Y. Wang, R. Zheng, J. Lu, X. Li, Z. Chen, X. Zhang, Y. Zhang, L. Liang, and Y. Zeng, Appl. Phys. Lett. **121**, 083901 (2022).
12) M. Koyama and M. Ichimura, Jpn. J. Appl. Phys. **58**, 128003 (2019).
13) N. Park, K. Sun, Z. Sun, Y. Jing, and D. Wang, J. Mater. Chem. C **1**, 7333 (2013a).
14) N. Kato and M. Sugiyama, Jpn. J. Appl. Phys. **59**, 101004 (2020).
15) R. Zheng, J. Lu, Y. Wang, Z. Chen, X. Zhang, X. Li, L. Liang, L. Qin, and Y. Zeng, Appl. Phys. Lett. **121**, 103902 (2022).
16) S. I. Maximenko, J. E. Moore, C. A. Affouda, and P. P. Jenkins, Sci. Rep. **9**, 10892 (2019).
17) M. Kim, J. H. Seo, U. Singisetti, and Z. Ma, J. Mater. Chem. C **5**, 8338 (2017).
18) S. Chakrabarty and K. Chatterjee, V. U. **13**, 245 (2009).
19) K. Yang, J. R. East, and G. I. Haddad, Solid-State Electron. **36**, 321 (1993).
20) E. Danielsson, C. M. Zetterling, M. Östling, D. Tsvetkov, and V. Dmitriev, J. Appl. Phys. **91**, 2372 (2002).
21) D. S. Atlas, ATLAS User's Manual Silvaco Inc., Santa Clara, 2019, p. 508.
22) N. Park, K. Sun, Z. Sun, Y. Jing, and D. Wang, J. Mater. Chem. C **1**, 7333 (2013b).
23) S. Chen, T. Kuo, Y. Lin, and H. Lin, Thin Solid Films. **519**, 4944 (2011).